NUMERICAL SIMULATION OF DETONATION PROCESS IN A TUBE

Hyungwon KIM,[†]   **Frank K. LU,**[‡]
Dale A. ANDERSON[‡]   **Donald R. WILSON**[‡]

Abstract

A two-dimensional time-accurate numerical model to simulate hydrogen–air detonation wave propagation and reflection was developed. To construct an efficient numerical tool, while maintaining a reasonable accuracy, a two-step global model was selected and validated for a hydrogen–air mixture. The inherent stiffness in the chemical reaction model was properly taken care of by a point-implicit treatment of source terms, together with the application of a "local ignition averaging model" to each mesh where ignition starts. Calculations were performed to select a scheme with adequate temporal and spatial resolution for modeling the physical process for practical calculations. Calculations were compared against Chapman–Jouguet theory as well as against experiment.

Key Words: Detonation, deflagration-to-detonation transition, Chapman–Jouguet, ignition

1   INTRODUCTION

Despite the destructive nature of detonations, there is considerable interest recently in exploiting detonations for certain applications, such as in propulsion [1] and in high-enthalpy ground test facilities [2]. While there are many unresolved fundamental issues regarding initiation, transition and propagation, for example, numerical modeling for obtaining engineering solutions are sought for the above-mentioned applications. Time-accurate computational fluid dynamics (CFD) methods can be used to perform cycle analysis and performance optimization of pulse detonation engines from the simulations of the corresponding flow fields with variations in design parameters. These methods can also be used to support the development of detonation drivers.

An unsteady numerical simulation model for the above purposes, emphasizing accuracy and efficiency, is described.   The objective is to construct a two-dimensional time-accurate numerical simulation model, efficient enough for design parametric studies

while maintaining a reasonable accuracy. The model is constructed to formulate the physical phenomena as precisely as possible, including chemical and thermal non-equilibrium, and to numerically solve the resulting mathematical formulation as accurately as possible. Novel aspects of this work include a combination of point-implicit treatment and a "local ignition averaging model" (LIAM) applied to the global two-step reaction model for efficient time-accurate solution of a propagating detonation wave. The partition of internal energy is based on the two-temperature model, and the vibrational energy of each species is obtained by subtracting out fully-excited translational and rotational energy from the total internal energy. Roe's flux-difference split scheme is combined with a Runge–Kutta integration scheme for an accurate capture of the shock wave in space and in time. Extensive calculations are performed with numerical schemes of different orders in space and time, and with different mesh sizes to select the proper scheme and mesh size to provide adequate resolution of the physical process. The present model is validated by comparing the calculated data with those obtained from Chapman–Jouguet theory and experiments.

2   MATHEMATICAL FORMULATION

2.1   Governing Equations

The time-dependent conservation equations governing an inviscid, non-heat-conducting, reacting gas flow in which thermal nonequilibrium is modeled with a two-

temperature approximation are written in the conservation law form. This form is advantageous in numerical simulations since it can correctly capture shock waves [3]. For a two-dimensional Cartesian coordinate system, the system of equations take the form

$$\frac{\partial U}{\partial t} + \frac{\partial F}{\partial x} + \frac{\partial G}{\partial y} = S \qquad (1)$$

where U is the vector of conserved variables, F and G are the convective flux vectors, and S is the vector of source terms. Each vector is written as

$$U = \begin{bmatrix} \rho_s \\ \rho u \\ \rho v \\ \rho e_v \\ \rho E \end{bmatrix}, \quad F = \begin{bmatrix} \rho_s u \\ \rho u^2 + p \\ \rho uv \\ \rho u e_v \\ \rho u E + pu \end{bmatrix},$$

$$G = \begin{bmatrix} \rho_s v \\ \rho uv \\ \rho v^2 + p \\ \rho v e_v \\ \rho v E + pv \end{bmatrix}, \quad S = \begin{bmatrix} w_s \\ 0 \\ 0 \\ w_v \\ 0 \end{bmatrix} \qquad (2)$$

The subscript $s = 1, 2, 3, \ldots, N_s$ where N_s is the number of species. The first N_s rows represent species continuity, followed by the two momentum conservation equations for the mixture. The next row describes the rate of change in the vibrational energy, and the final row is the total energy conservation equation. The terms u and v are the velocities in the x and y directions respectively, ρ is the mixture density, p is the pressure, e_v is the vibrational energy, E is the total energy per unit mass of mixture, ρ_s is the s-th species density, w_s is the mass production rate of species s per unit volume, and w_v is the vibrational energy source term which is defined as

$$w_v = \sum_s Q_{vs} + \sum_s w_s e_{d,s} \qquad (3)$$

The first term on the RHS, Q_{vs}, represents the vibrational energy exchange rate of species s due to the relaxation process with translational energy. The second term on the RHS, $w_s e_{d,s}$, represents the amount of vibrational energy gained or lost due to production or depletion of species s from chemical reactions.

2.2 Thermodynamic Properties

In general, the internal energy of each species includes a portion of the internal energy in thermodynamic equilibrium and the remaining portion in a nonequilibrium state. The equilibrium portion of the internal energy is the contribution due to translation and internal modes that can be assumed to be in equilibrium at the translational temperature T. The remaining nonequilibrium portion is the contribution due to internal modes that are not in equilibrium at the translational temperature T, but may be assumed to satisfy a Boltzman distribution at a different temperature.

For the temperature range of interest, the rotational mode is assumed to be fully excited and in equilibrium with the translational temperature T, while the electronic excitation and free electron modes can be safely ignored. The vibrational mode remains as the only energy mode that could be in nonequilibrium with the translational temperature T. Thus, the species internal energy based on a two-temperature model can be written as

$$e_s = e_{eq,s}(T) + e_{v,s}(T_v) \qquad (4)$$

where $e_{eq,s}$ is the equilibrium portion of the internal energy and $e_{v,s}$ is the vibrational energy which is not in thermodynamic equilibrium. The equilibrium portion of the energy can be further defined as

$$e_{eq,s} = \int_{T_{ref}}^{T} \left(C_{v,t}^s + C_{v,r}^s \right) d\tau + e_{s,o} \qquad (5)$$

where T_{ref} is the reference temperature, $e_{s,o}$ is the energy of formation at the reference temperature, and $C_{v,t}^s$ and $C_{v,r}^s$ are the translational and rotational portion of the specific heat at constant volume, respectively. Since the translational and rotational modes are assumed to be fully excited, $C_{v,t}^s$ and $C_{v,r}^s$ can be written as

$$C_{v,t}^s = 1.5\bar{R}/M_s \qquad (6)$$

$$C_{v,r}^s = \begin{bmatrix} \bar{R}/M_s, \text{diatomic molecule} \\ 1.5\bar{R}/M_s, \text{polyatomic molecule} \end{bmatrix} \qquad (7)$$

where $\bar{R}$ is the universal gas constant and M_s is the molecular weight of species s. The energy of formation $e_{s,o}$ can be obtained from readily available heat of formation data as

$$e_{s,o} = h_{s,o} - \frac{\bar{R}}{M_s} T_{ref} \qquad (8)$$

Therefore, the equilibrium portion of energy can be written as

$$e_{eq,s}(T) = K_s \frac{\bar{R}}{M_s}(T - T_{ref}) - \frac{\bar{R}}{M_s} T_{ref} + h_{s,o} \qquad (9)$$

where $K_s = 1.5, 2.5, 3.0$ for monatomic, diatomic or linear polyatomic, and nonlinear polyatomic species respectively.

The heat capacity of the vibrational energy mode can be obtained from the fact that the translational and rotational heat capacities are independent of temperature. This can be evaluated by utilizing a readily available curve fit for total heat capacity evaluated at the temperature T_v and subtracting out the constant contributions from the translation and rotational heat capacities, namely,

$$C_{v,v}^s(T_v) = C_v^s(T_v) - C_{v,t}^s - C_{v,r}^s \qquad (10)$$

where

$$C_v^s(T_v) = C_p^s(T_v) - \frac{\bar{R}}{M_s}$$

C_v^s and C_p^s are specific heats at constant volume and constant pressure respectively. Curve fit data for $C_p^s(T)$ can be found in the following form [4]:

$$C_p^s(T) = \frac{\bar{R}}{M_s} \sum_{k=1}^{5} A_k^s T^{k-1} \qquad (11)$$

Therefore, $C_{v,v}^s$ can be obtained as follows:

$$C_{v,v}^s(T_v) = \begin{bmatrix} \dfrac{\bar{R}}{M_s}\left(\displaystyle\sum_{k=1}^{5} A_k^s T_v^{k-1} - \dfrac{7}{2}\right), \text{diatomic} \\[2em] \dfrac{\bar{R}}{M_s}\left(\displaystyle\sum_{k=1}^{5} A_k^s T_v^{k-1} - 4\right), \text{polyatomic} \end{bmatrix}$$

$$(12)$$

The species vibrational energy $e_{v,s}$ can be obtained by integrating $C_{v,v}^s$ such that

$$e_{v,s}(T_v) = \int_{T_{ref}}^{T_v} C_{v,v}^s(\tau)d\tau \qquad (13)$$

2.3 Chemical Kinetics

For accurate modeling of a detonation wave, especially in the detonation front where rapid chemical reactions take place in the shock compressed region, species continuity equations based on the chemical kinetics should be solved together with the fluid dynamic equations to account for possible chemical nonequilibrium. The mass production rate of species s from chemical reactions can be written as [5]

$$w_s = M_s \sum_{r=1}^{N_r} (\beta_{s,r} - \alpha_{s,r})(R_{f,r} - R_{b,r}) \qquad (14)$$

where M_s is the molecular weight of species s, N_r is the number of reactions, $\alpha_{s,r}$ and $\beta_{s,r}$ are the stoichiometric coefficients for reactants and products, respectively, in the r reaction. The forward and backward reaction rate of the r reaction, $R_{f,r}$ and $R_{b,r}$, respectively, are defined by

$$R_{f,r} = 1000\left[K_{f,r}\prod_{s=1}^{N_s}(0.001\rho_s/M_s)^{\alpha_{s,r}}\right]$$

$$(15)$$

$$R_{b,r} = 1000\left[K_{b,r}\prod_{s=1}^{N_s}(0.001\rho_s/M_s)^{\beta_{s,r}}\right]$$

The factors 1,000 and 0.001 are required to convert from CGS to MKS units, since most reaction rate data in the literature are found in CGS units.

The forward reaction rate coefficient can be expressed by

$$K_{f,r} = A_{f,r}T^{N_{f,r}}\exp(-E_{f,r}/\bar{R}T) \qquad (16)$$

where $E_{f,r}$ is the activation energy of the r-th forward reaction. The values of parameters $A_{f,r}$, $N_{f,r}$, $E_{f,r}$ are usually found tabulated according to the reactions involved. The backward reaction rate coefficient is evaluated using the equilibrium constant for the reaction such that

$$K_{b,r} = K_{f,r}/K_{c,r} \qquad (17)$$

2.4 Vibrational Energy Relaxation

The energy exchange between vibrational and translational modes due to intermolecular collisions is well described by the Landau–Teller formulation where it is assumed that the vibrational level of a molecule can change by only one quantum level at a time [6, 7]. The resulting energy exchange rate is given by

$$Q_{v,s} = \rho_s\frac{e_{v,s}^*(T) - e_{v,s}}{<\tau_s>} \qquad (18)$$

where $e_{v,s}^*(T)$ is the vibrational energy per unit mass of species s evaluated at the local translational–rotational temperature, and $<\tau_s>$ is the averaged Landau–Teller relaxation time of species s given by [5]

$$<\tau_s> = \sum_{j=1}^{N_s} n_j\tau_{sj} \bigg/ \sum_{j=1}^{N_s} n_j \qquad (19)$$

where τ_{sj} is the vibrational–translational relaxation time of species s caused by intermolecular collision with species j, and n_j is number density of species j.

The Landau–Teller interspecies relaxation time τ_{sj} can be obtained in seconds using the Millikan–White semi-empirical expression [8]

$$\tau_{sj} = \frac{1}{p}\exp\left[A_{sj}\left(T^{-1/3} - 0.015\mu_{sj}^{1/4}\right) - 18.42\right]$$

$$(20)$$

where p = pressure in atm, $A_{sj} = 1.16 \times 10^{-3} \mu_{sj} \theta_{sj}$, $\mu_{sj} = M_s M_j / (M_s + M_j)$ is the reduced mass, and θ_{sj} = characteristic vibrational temperature of a harmonic oscillator. The vibrational energy relaxation rate can be simplified using [5]

$$\sum_s \rho_s \frac{e_{v,s}^* - e_{v,s}}{< \tau_s >} \approx \sum_s \rho_s C_{v,v}^s \frac{T - T_v}{< \tau_s >}$$
$$\approx \frac{\rho C_{v,v}}{\tau v}(T - T_v) \qquad (21)$$

where

$$\frac{1}{\tau_v} = \frac{\sum_s \rho_s / (M_s < \tau_s >)}{\sum_s \rho_s / M_s}$$

This approximation reduces the number of species dependent parameters and simplifies the evaluation of the vibrational relaxation as a single relaxation term multiplied by the difference in the translational and vibrational temperature. When a point implicit formulation is used on the source terms in the numerical algorithm, the above approximation greatly simplifies an implicit treatment of the temperature difference which drives the relaxation process.

3 NUMERICAL FORMULATION

3.1 Finite-Volume Formulation

A discretized set of equations is derived from the governing partial differential equations using the finite-volume method. The advantage of this method is its use of the integral form of the equations, which ensures conservation, and allows the correct treatment of discontinuities [3]. In the following derivation, the cell-centered approach will be described.

For an arbitrary volume Ω, enclosed by a boundary σ, the governing equations in integral form can be written as

$$\frac{\partial}{\partial t} \iiint U \, d\Omega + \oint_\sigma \vec{H} \cdot \vec{n} \, d\sigma = \iiint S \, d\Omega \qquad (22)$$

where

$$\vec{H} = (F, G)$$

The unit vector $\vec{n}$ is normal to the infinitesimal area $d\sigma$ and points outwards. The first step to discretize the above equation is to introduce volume averaged values of the conserved variables and the source term as follows:

$$< U > = \frac{1}{\Omega} \iiint U \, d\Omega, \quad < S > = \frac{1}{\Omega} \iiint S \, d\Omega \quad (23)$$

These volume averaged variables are substituted into the integral form of the governing equations to yield

$$\frac{\partial}{\partial t}(< U > \Omega) + \oint_\sigma (F, G) \cdot \vec{n} \, d\sigma = < S > \Omega \qquad (24)$$

For a two-dimensional Cartesian coordinate system where the computational cell is defined by two constant lines in both the x and y directions, the surface integral can be split into four contributions, one from each bounding surface. When the index of the cell centered variables is (i, j), Eq. (24) can be written as

$$\oint_\sigma (F, G) \cdot \vec{n} \, d\sigma = \iint_{\sigma_{i+1/2}} F \, d\sigma + \iint_{\sigma_{i-1/2}} F \, d\sigma$$
$$+ \iint_{\sigma_{j+1/2}} G \, d\sigma + \iint_{\sigma_{j-1/2}} G \, d\sigma$$
$$(25)$$

Area-averaged values of fluxes can be defined such that

$$< F >_{i+1/2} = \frac{1}{\sigma_{i+1/2}} \iint_{\sigma_{i+1/2}} F \, d\sigma,$$
$$< G >_{j+1/2} = \frac{1}{\sigma_{j+1/2}} \iint_{\sigma_{j+1/2}} G \, d\sigma \qquad (26)$$

where the bounding surface areas $\sigma_{i+1/2}, \sigma_{j+1/2}$ actually represent cell face lengths in the two-dimensional Cartesian coordinate system. After substituting these definitions of averaging into the Eq. (24) and dropping the brackets, the following discrete form of the conservation equations written in a two-dimensional Cartesian coordinate system can be obtained:

$$\frac{\partial U_{i,j}}{\partial t} = -\left(F_{i+1/2} \frac{\sigma_{i+1/2}}{\Omega_{i,j}} - F_{i-1/2} \frac{\sigma_{i-1/2}}{\Omega_{i,j}} \right)$$
$$- \left(G_{j+1/2} \frac{\sigma_{j+1/2}}{\Omega_{i,j}} - G_{j-1/2} \frac{\sigma_{j-1/2}}{\Omega_{i,j}} \right)$$
$$+ S_{i,j} \qquad (27)$$

3.2 Point Implicit Time Integration

Nonequilibrium flows involving finite-rate chemistry and thermal energy relaxation often can be very difficult to solve numerically because of stiffness. The stiffness in terms of the time scale can be defined as the ratio of the largest to the smallest time scale such that

$$\text{Stiffness} = \tau_{\text{largest}} / \tau_{\text{smallest}}$$

where τ can be any characteristic time in the flow field. For reactive flow problems, there can be several chemical time scales and relaxation time scales in addition to the fluid dynamic time scale associated with

convection. The stiffness parameter can be as high as $\mathcal{O}(10^6)$. The point implicit formulation evaluating the source terms at time level $(n+1)$ has been an effective method used to numerically integrate stiff systems [9]. The point implicit treatment is known to reduce the stiffness of the system by effectively rescaling all the characteristic times in the flow fields into the same order of magnitude.

Equation (27) is rewritten here with the source terms evaluated at the time level $(n+1)$ as

$$\frac{\partial U_{i,j}}{\partial t} = -\left(F^n_{i+1/2}\frac{\sigma_{i+1/2}}{\Omega_{i,j}} - F^n_{i-1/2}\frac{\sigma_{i-1/2}}{\Omega_{i,j}}\right)$$
$$-\left(G^n_{j+1/2}\frac{\sigma_{j+1/2}}{\Omega_{i,j}} - G^n_{j-1/2}\frac{\sigma_{j-1/2}}{\Omega_{i,j}}\right) + S^{n+1}_{i,j}$$
(28)

The source vector is then linearized about the present time level such that

$$S^{n+1} = S^n + \left(\frac{\partial S}{\partial U}\right)^n \Delta U \qquad (29)$$

When simple Euler time integration is used, substituting this linearization into the above equation and rearranging yields

$$\left[\frac{1}{\Delta t} - \left(\frac{\partial S}{\partial U}\right)^n\right]\Delta U = -F^n_{i+1/2}\frac{\sigma_{i+1/2}}{\Omega_{i,j}}$$
$$+F^n_{i-1/2}\frac{\sigma_{i-1/2}}{\Omega_{i,j}} - G^n_{j+1/2}\frac{\sigma_{j+1/2}}{\Omega_{i,j}}$$
$$+ \ G^n_{j-1/2}\frac{\sigma_{j-1/2}}{\Omega_{i,j}} + S^n_{i,j} \qquad (30)$$

These equations can be evaluated to get ΔU entirely at the current time level at the expense of matrix inversion containing the source term Jacobian.

Temporal accuracy can be added using Runge–Kutta integration schemes instead of first-order accurate Euler integration. The two-step explicit Runge–Kutta time integration scheme can be written as

$$U^{n+\frac{1}{2}} = U^n + \gamma_1 \Delta U^n$$
$$U^{n+1} = U^{n+\frac{1}{2}} + \gamma_2 \Delta U^{n+\frac{1}{2}} + \zeta_2 \Delta U^n \qquad (31)$$

where $\gamma_1 = 1.0$, $\gamma_2 = 0.5$, and $\zeta_2 = $ -0.5, and the three step scheme is given by

$$U^{n+\frac{1}{3}} = U^n + \gamma_1 \Delta U^n$$
$$U^{n+\frac{2}{3}} = U^{n+\frac{1}{3}} + \gamma_2 \Delta U^{n+\frac{1}{3}} + \zeta_2 \Delta U^n \qquad (32)$$
$$U^{n+1} = U^{n+\frac{2}{3}} + \gamma_3 \Delta U^{n+\frac{2}{3}} + \zeta_3 \Delta U^{n+\frac{1}{3}}$$

where $\gamma_1 = 8/15$, $\gamma_2 = 5/12$, $\gamma_3 = 3/4$, and $\zeta_2 = -17/60$, $\zeta_3 = -5/12$.

3.3 Flux-Difference Split Algorithm

The basic feature of the flux-difference split algorithm is the solution of a local Riemann problem at the cell interface to determine the cell-face flux. An approximate Riemann problem is used with Roe's scheme, originally developed for a perfect gas [10] and later extended to a thermo-chemical non-equilibrium gas [11]. The flux-difference scheme used here is based on the latter method.

The approximate Rieman solver is implemented by computing the cell face flux as a summation of the contributions from each wave component,

$$F_{i+1/2} = \frac{1}{2}\left(F_R + F_L\right) - \frac{1}{2}\sum_{i=1}^{N_s+4} \hat{\alpha}_i \left|\hat{\lambda}_i\right| \hat{E}_i$$
$$= \frac{1}{2}\left(F_R + F_L\right) - \frac{1}{2}\left([[F]]_A + [[F]]_B + [[F]]_C\right)$$
(33)

where subscripts R and L represent the right and left state respectively, λ_i are eigenvalues, E_i are eigenvectors, α_i are corresponding wave strengths, and $^\wedge$ indicates Roe-averaged quantities. The $[[F]]_A$ term corresponding to the repeated eigenvalues $\lambda_i = u$ can be written as

$$[[F]]_A = \left([[\rho]] - \frac{[[p]]}{\hat{a}^2}\right)|\hat{u}| \begin{bmatrix} \hat{\rho}_i \\ \hat{u} \\ \hat{v} \\ \hat{e}_v \\ \hat{H} - \hat{a}^2/(\hat{\gamma}-1) \end{bmatrix}$$
$$+ \hat{\rho}|\hat{u}| \begin{bmatrix} [[\rho_i/\rho]] \\ 0 \\ [[v]] \\ [[e_v]] \\ \theta \end{bmatrix} \qquad (34)$$

where

$$[[(\cdot)]] = (\cdot)_R - (\cdot)_L$$
$$\theta = [[e_v]] - \sum_{i=1}^{N_s} \hat{\Psi}_i[[\rho_i/\rho]] + \hat{v}[[v]]$$
$$\Psi_i \equiv \frac{1}{\tilde{\gamma}-1}\frac{\partial p}{\partial \rho_i} = \frac{R_i T}{\tilde{\gamma}-1} - e_{eq,i} + \frac{u^2+v^2}{2}$$
$$\tilde{\gamma} = \frac{\tilde{C}_p}{\tilde{C}_v} = \frac{C_{p,t} + C_{p,r}}{C_{v,t} + C_{v,r}}$$
$$R = \bar{R}/M_s$$

The $[[F]]_B$ and $[[F]]_C$ terms which are contributions from the eigenvalues $\lambda_i = u \pm a$, are found to be

$$[[F]]_{B,C} = \frac{1}{2\,\hat{a}^2} \left([[p]] \pm \hat{\rho}\,\hat{a}[[u]] \right) (\hat{u} \pm \hat{a}) \begin{bmatrix} \hat{\rho}_i \\ \hat{u} \pm \hat{a} \\ \hat{v} \\ \hat{e}_v \\ \hat{H} \pm \hat{u}\hat{a} \end{bmatrix}$$
(35)

For added spatial accuracy, a higher-order approximation using the MUSCL approach can be applied. When the MUSCL approach is employed, the primitive variables of the right and left states at the cell interface are evaluated using the following extrapolation formulas [3]

$$q_{i+1/2}^L = q_i + \frac{1-\kappa}{4}\,\bar{\delta}^+ q_{j-1/2} + \frac{1+\kappa}{4}\,\bar{\delta}^- q_{j+1/2}$$
$$q_{i+1/2}^R = q_{i+1} - \frac{1+\kappa}{4}\,\bar{\delta}^+ q_{j+1/2} - \frac{1-\kappa}{4}\,\bar{\delta}^- q_{j+3/2}$$
(36)

where q is any primitive variable, the superscripts L and R represent left and right extrapolation respectively, and κ determines the type of extrapolation method such that

$$\kappa = \begin{cases} -1 & \text{2nd-order upwind scheme} \\ 1/3 & \text{3rd-order upwind scheme} \\ 1 & \text{2nd-order classic centered scheme} \end{cases}$$
(37)

In the above equations, the slopes of the variables are limited to prevent nonphysical oscillations and to preserve the TVD (Total Variation Diminishing) property. The limited slopes can be written using the minmod limiter as follows:

$$\bar{\delta}^- q_{i+1/2} = \min \text{mod}(\delta\,q_{i+1/2},\,\omega\delta\,q_{i-1/2})$$
$$\bar{\delta}^+ q_{i+1/2} = \min \text{mod}(\delta\,q_{i+1/2},\,\omega\delta\,q_{i+3/2})$$
(38)

The minmod limiter is a function that selects the smallest number from a set when all have the same sign but is zero if they have different signs such that

$$\min \text{mod}(x,y) = \begin{cases} x \text{ if } |x| < |y| & \text{and } xy > 0 \\ y \text{ if } |x| > |y| & \text{and } xy > 0 \\ 0 \text{ if } & xy < 0 \end{cases}$$
(39)

with the limits on ω given as

$$1 \leq \omega \leq (3-\kappa)/(1-\kappa)$$
(40)

3.4 Temperature Calculation

The conserved variables at each cell center are updated using Eq. (30) by a matrix inversion. From these conserved variables, new values of the primitive variables, ρ_s, u, v, e_v, E, are easily obtained. However, to close the problem, the temperature and vibrational temperature are determined at each iteration cycle. A Newton–Raphson method is used to obtain the temperature in the following manner [5, 12]:

$$T^{(k+1)} = T^{(k)} + \frac{\rho e - \sum_s \rho_s e_s \left(T^{(k)}, T_v^{(k)} \right)}{\rho C_{v,tr}}$$

$$T_v^{(k+1)} = T_v^{(k)} + \frac{\rho e_v - \sum_s \rho_s e_{v,s} \left(T^{(k)} \right)}{\rho C_{v,v}}$$
(41)

While the total internal energy e and vibrational energy e_v are directly obtained from the updated conservative variables, the species internal energies e_s and the species vibrational energies $e_{v,s}$ are calculated from the gas model using the current values of both temperatures. The iteration is carried out until converged values of both temperatures are obtained.

4 VALIDATION STUDIES

4.1 H₂–Air Reaction Model and Local Ignition Averaging

The two-step Rogers–Chinitz reaction model is used in this study [13]. This model was developed to represent H_2–air chemical kinetics with as few reaction steps as possible while still giving reasonably accurate global results. This model consists of the following two steps:

$$H_2 + O_2 \longleftrightarrow 2OH$$
$$2OH + H_2 \longleftrightarrow 2H_2O$$
(42)
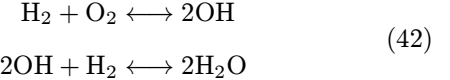
where the forward reaction rate constants are given by

$$K_{f,r} = A_{f,r}(\phi)\,T^{N_{f,r}} \exp(-E_{f,r}/\bar{R}T)$$
(43)

and the pre-exponential $A_{f,r}(\phi)$ is a function of the equivalence ratio ϕ, the fuel-to-air ratio divided by the stoichiometric fuel-to-air ratio. Values of the parameters used in this model are

$$\begin{bmatrix} A_{f,1}(\phi) = [8.917\phi + (31.433/\phi) - 28.950]\,10^{47} \\ N_{f,1} = -10 \\ E_{f,1} = 4\,865 \quad \text{cal/mole} \end{bmatrix}$$
(44)

$$\begin{bmatrix} A_{f,2}(\phi) = [2.000 + (1.333/\phi) - 0.833\phi]\,10^{64} \\ N_{f,2} = -13 \\ E_{f,2} = 42\,500 \quad \text{cal/mole} \end{bmatrix}$$
(45)

The backward reaction rate can be obtained from

$$K_{b,r} = K_{f,r}/K_{c,r} \qquad (46)$$

where the equilibrium constant $K_{c,r}$ is given by

$$K_{c,r} = A_{c,r}\, T^{N_{c,r}} \exp(-E_{c,r}/\bar{R}T) \qquad (47)$$

where

$$\begin{bmatrix} A_{c,1} = 26.164 \times 10^3 & \text{cm}^3/\text{mole} \cdot \text{s} \\ N_{c,1} = 0 \\ E_{c,1} = 17\,867 & \text{cal/mole} \end{bmatrix} \qquad (48)$$

$$\begin{bmatrix} A_{c,2} = 2.682 \times 10^{-3} & \text{cm}^6/\text{mole}^2 \cdot \text{s} \\ N_{c,2} = 1 \\ E_{c,2} = -137\,930 & \text{cal/mole} \end{bmatrix} \qquad (49)$$

This model is valid for initial temperatures of 1000–2000 K and equivalence ratios of 0.2–2. Since the chemistry model is not valid below 1000 K, an ignition temperature must be specified. Nitrogen is also counted as a collisional partner in the thermodynamic model and the relaxation process, but not included in the chemical reaction model since the maximum temperature in the hydrogen–air reaction does not reach the dissociation temperature of nitrogen.

Before an actual calculation using the flow solver is made, the chemical kinetic model must be examined to see how each species concentration is changing, and on what time scale. This may provide some insight into the stiffness of the system and some clues for establishing a flow solver time step that permits species concentrations to follow the correct kinetics.

The mass production rate, Eq. (14), can be independently integrated using the reaction data in Eqs. (43)–(49) to yield the species mass fraction history. A typical result obtained using a Runge–Kutta integration method is in Fig. 1. The mass fraction of OH is seen to rise very rapidly as soon as the ignition starts. The OH production reaction is instantaneous at its initial stage and goes to equilibrium very quickly in less than 10^{-11} s. After that, the reactions seem to remain in equilibrium until the H_2O production reaction begins around 10^{-9} s. It is interesting to note that all these major changes in species concentrations take place within the first 10^{-7} s, a time interval that is a typical fluid dynamic time step in the calculations. Moreover, the integration time step should remain at or below 10^{-12} s to ensure stable integration using the Runge–Kutta scheme and to properly follow the chemical kinetics. This shows the stiffness of the chemical reaction model.

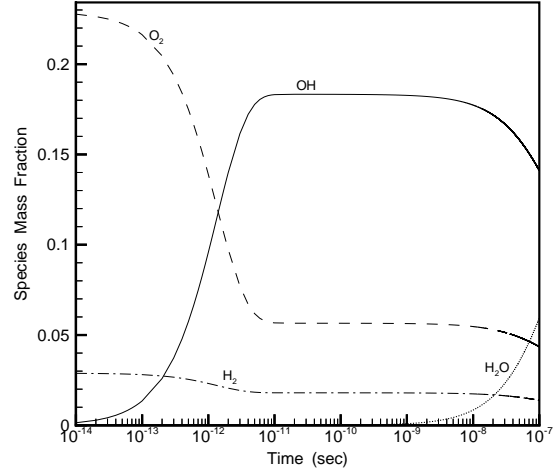From the above observation, it could be deduced that the integration time step for the flow solver

Fig.1: Species mass fraction history from chemical kinetics.

should be less than 10^{-12} s to properly include the chemical kinetics. Moreover, it should be much less than this order in regions of OH production. However, it is practically impossible to use this small time step in the flow solver. When using 10^{-12} s as a flow solver time step, 10^9 integration steps might be needed to solve a typical detonation wave propagation problem which has a time scale of interest of 10^{-3} s. This would result in 10^4 days of CPU time when 1 second of CPU time per computation cycle, which is a proper estimate for this code on a typical front-end workstation, is assumed. Fortunately, however, most of this stiffness problem can be taken care of by the point implicit treatment of source terms, through effectively rescaling all the characteristic time scales involved. Thus, a typical fluid dynamic time step of the order of 10^{-7} s can be safely used throughout the calculation, since the species production rates during this time interval can be properly treated by the effective rescaling of the chemical reaction time scale.

However, the very first time step where all the drastic changes take place within that short period of time cannot be properly described by rescaling time alone. Another special treatment for the igniting cell is needed to be able to use a typical flow solver time step. For this purpose, a "local ignition averaging model" (LIAM) is proposed. The basic idea for this model comes from the fact that the species mass fractions are changing drastically in a very short period as soon as ignition starts and reaches equilibrium soon afterwards. LIAM separates the cell in which the ignition condition is met and then integrates the chemical

kinetics equations alone for that cell. A time step less than 10^{-12} s is used in the integration within the interval of the flow solver time step. The average production rate of each species during this time interval is then estimated using

$$w_s = \Delta\rho_s/\Delta t_f \tag{50}$$

where $\Delta\rho_s$ is the density change of species s, obtained from a separate integration of the chemical kinetics equations during this time interval, and Δt_f is the flow solver time step. The average value of the forward reaction rate for each reaction during this interval can be estimated from

$$R_{f,1} = -W_{O_2}/M_{O_2}, \qquad R_{f,2} = W_{OH}/2M_{OH} \tag{51}$$

These terms must be obtained for calculating the source term Jacobian. Here, backward reaction rates during this first reaction time step are assumed to be zero.

LIAM turns out to work well together with the point implicit scheme to accurately describe chemical kinetics in the flow solver using a typical flow solver time step of 10^{-7} s. Figure 2 shows calculated results of the species mole fraction history at a fixed location inside the detonation chamber initially filled with hydrogen–air mixture. Excellent agreement can be seen with the equilibrium concentration data [14]. This assures that the chemical kinetics are properly modeled and coupled to the flow solver.
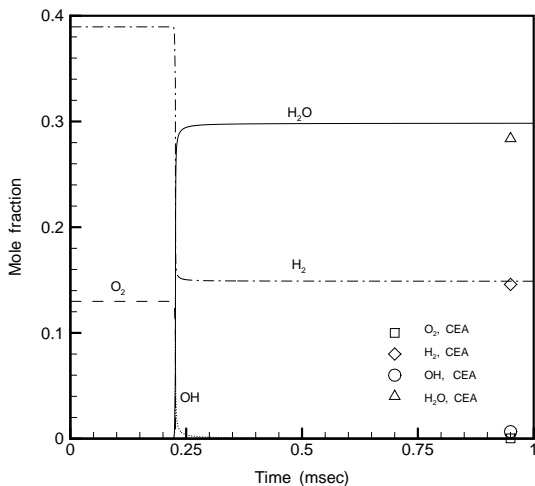
Fig.2: Species mole fraction history from the flow solver.

4.2 Spatial and Temporal Accuracy

Generally speaking, a higher-order scheme may yield more accurate results, in turn requiring more computing time. The present computer model accommodates the options to choose numerical schemes of both space and time integration up to third-order accuracy. For temporal accuracy, Euler integration for first-order, two-step Runge–Kutta (RK) integration for second-order, and three-step RK for third-order are contained in the model. For spatial accuracy, the MUSCL approach is used for higher-order approximations. This section examines the effect of the order of the numerical schemes on the predicted detonation wave. This can then be used to select the order of the scheme necessary to provide adequate resolution of the physical process.

Figure 3 is a comparison of detonation wave pressure profiles along a detonation chamber when numerical schemes of different order of accuracy are implemented. This figure compares detonation wave profiles, propagating into the quiescent hydrogen–air mixture initially at 1 atm. The higher-order calculation captures the higher peak pressure as expected. However, it is interesting to note that the second-order calculation is close to the third-order calculation, and that the overall shapes of the two waves are almost the same. This convergence trend can be seen more clearly in Fig. 4 which shows detonation wave velocities as a function of distance from the initiation point for each scheme. From this observation, a second-order calculation is a reasonable choice when efficiency and accuracy are considered together. Thus, a second-order accurate scheme in both space and time is employed to be used for further calculations, unless otherwise noted.

4.3 Mesh Convergence

A mesh convergence test is performed to determine the proper mesh size to insure accurate resolution of the physical process. The same configuration and parameters are used as before but with different mesh sizes. A second-order accurate scheme in both space and time is used throughout the calculation.

Figure 5 shows detonation wave profiles resulting from three different mesh sizes. Actual dimensional sizes of 5.0, 2.5, and 0.5 mm are used, respectively, in modeling a 2 m long tube with planar initiation. For calculations of both 5.0 and 2.5 mm mesh size, a time step of 10^{-7} seconds has been used successfully to yield stable solutions. However, for the smallest mesh size of 0.5 mm, a smaller time step of 5×10^{-8} s has been used, since a time step of 10^{-7} s does not yield a stable solution for this mesh size.

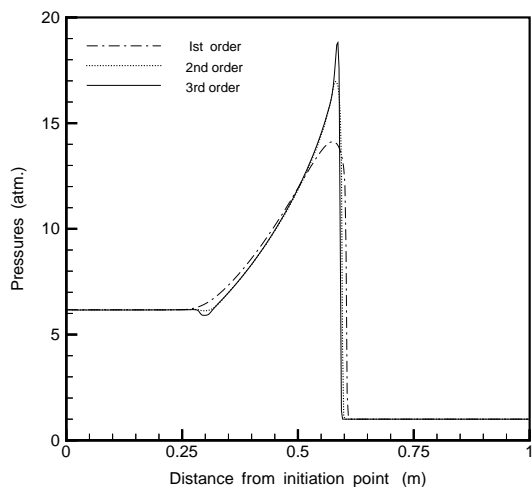The convergence trend can be seen clearly from

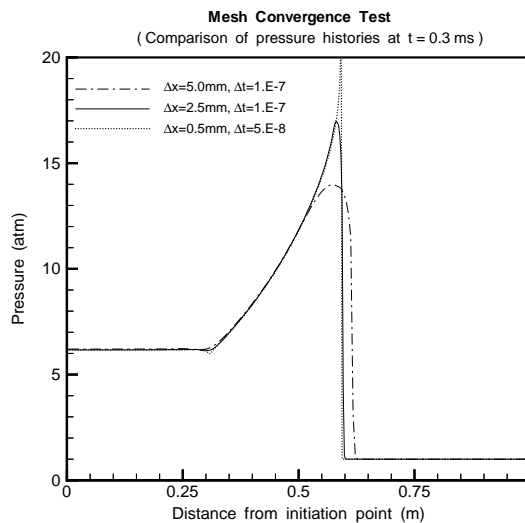Fig.3: Wave profiles from different orders of accuracy.

Fig.5: Wave profiles from different mesh sizes.

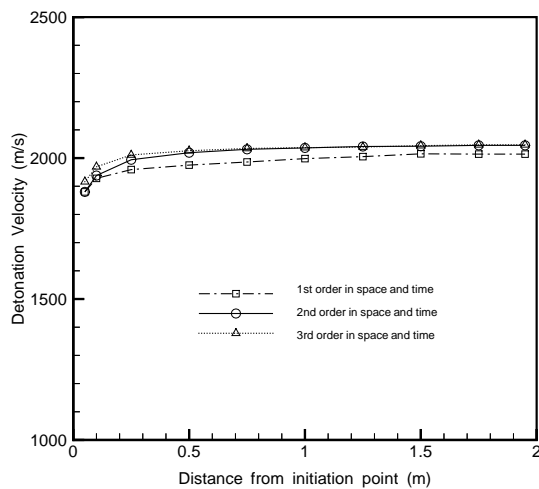mesh size, a mesh size of 2.5 mm is reasonable.

Fig.4: Detonation velocities from different orders of accuracy.

Fig. 6 which depict detonation wave velocities from the initiation point for each mesh size used. The results of the 2.5 mm mesh show values almost converged to the 0.5 mm mesh in both detonation velocity and overall wave shape. If we assume the computing time of 2.5 mm mesh case to be 1 CPU, then the corresponding computing times of 5.0 mm and 0.5 mm case will be about 1/4 CPU and 50 CPU, respectively, for a two-dimensional calculation. When we take into account accuracy as well as efficiency in choosing the

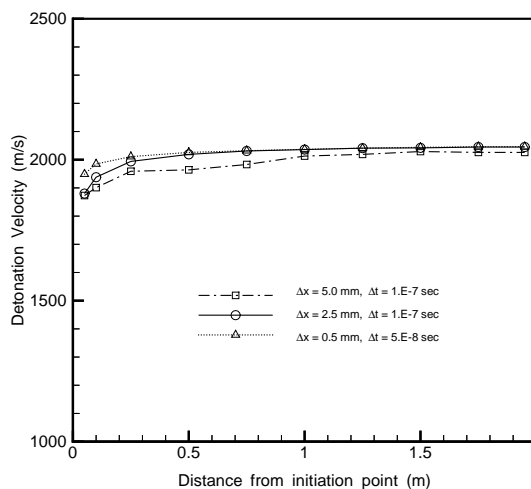
Fig.6: Detonation velocities from different mesh sizes.

4.4 Independence of the Geometry

The properties of fully-developed detonation waves should be the same regardless of the geometry involved whenever the initial condition and composition of the fuel–air mixture are the same. Four different calculations are performed here to confirm the results to follow this postulate. We take four cases with two kinds of geometry and two initiation methods, which are two-dimensional calculations with planar initia-

tion and with point initiation, and repeat the calculations for axisymmetric flow with the same initiation methods. The calculation domain is 68.5 cm × 3.75 cm for both and filled with a stoichiometric hydrogen–air mixture at 1 atm. Initiation occurs near the left-end wall.
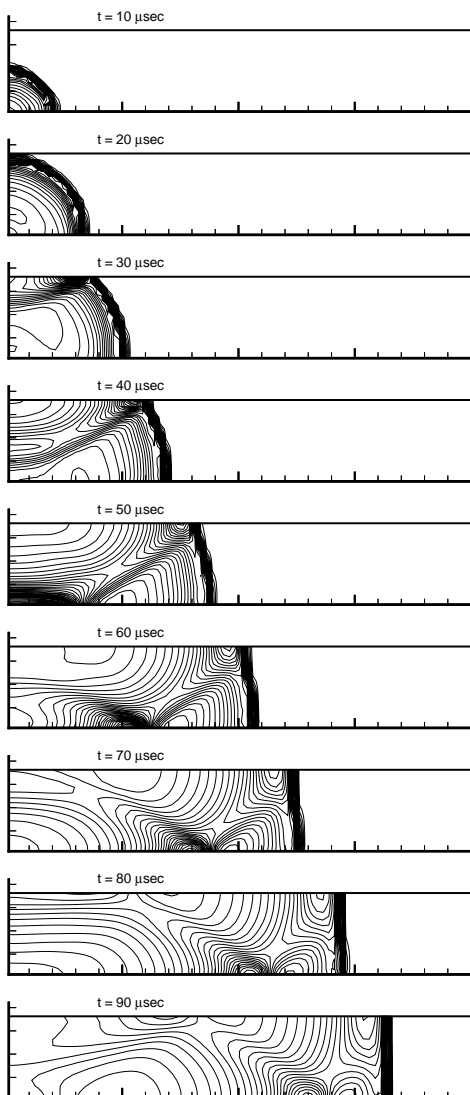

Fig.7: Point initiation in axisymmetric geometry.

Figure 7 shows pressure contour plots at specified times for a point initiation case in axi-symmetric geometry. The formation of a planar detonation wave is clearly captured. A planar wave can be observed to evolve from a spherical wave originated from a point initiation through the interactions of the reflecting waves.
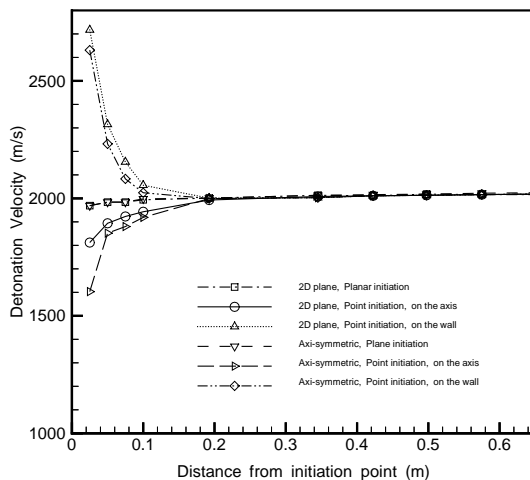
The calculated results are summarized in Figs. 8

Fig.8: Detonation velocities from different geometries in use.
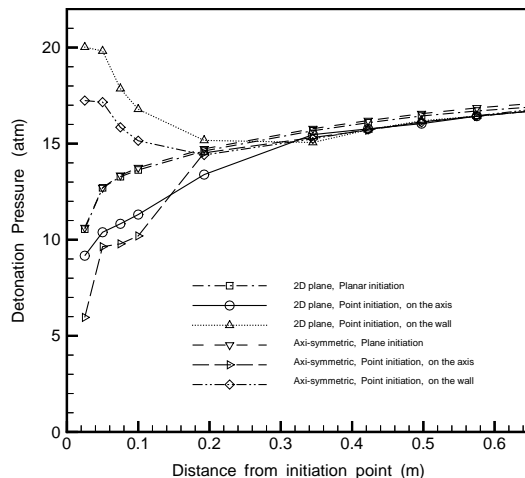

Fig.9: Detonation pressures from different geometries in use.

and 9. These figures show detonation wave velocities and the CJ plane pressures, respectively, along two different lines which are the lower boundary (actually, the centerline) and the upper wall. For point initiation cases, detonation velocities and pressures on the axis are observed to remain lower than those of planar initiation cases but increasing, while the detonation velocities and the pressures on the wall are much higher than those of planar initiation cases and decreasing until the formation of the planar wave. The higher
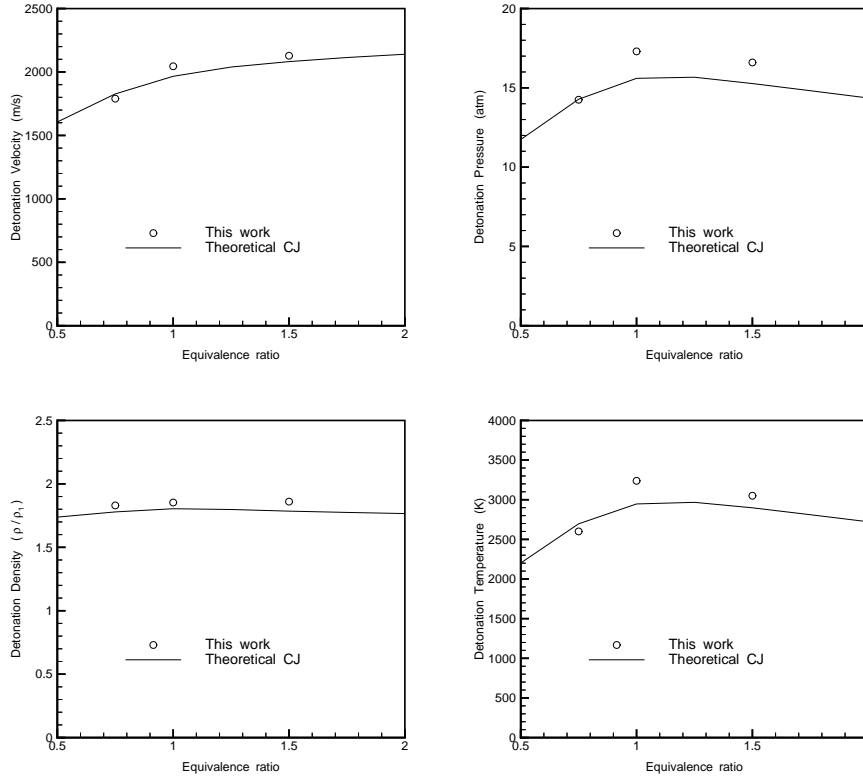
Fig.10: Comparison with CJ theory.

pressure and velocity on the wall are due to the reflection of the detonation wave. The detonation velocities and the pressures for all four cases are observed to converge to the same value at a certain distance from the initiation point where fully developed planar waves are formed, confirming the postulate stated above.

4.5 Comparison with Chapman–Jouguet Theory

The calculated detonation wave properties are compared with those obtained from CJ theory. Since the properties of the fully-developed detonation wave converges to the same value regardless of the geometry involved, as seen in the previous section, and since we are interested in the final converged state of the CJ condition, calculations can be properly performed on the one-dimensional planar geometry for the sake of efficiency. The computational domain is thus composed of a detonation tube of semi-infinite length filled with a stoichiometric hydrogen–air mixture initially at 1 atm and 298.15 K. The detonation is initiated just adjacent to the left-end wall, and the planar wave propagates to the right through the quiescent gas mixture. The detonation wave velocity, pressure, density,

and temperature as a function of distance from an initiation point are compared with the theoretical CJ values [14]. The converging trend of all the variables of the detonation wave is confirmed in each calculation of different equivalence ratios. These converged values can be compared to the theoretical CJ data. The results are summarized in Fig. 10, which depicts the converged values of each detonation variable with varying equivalence ratios, and compares these values with the theoretical CJ data. Excellent agreement between them is observed.

4.6 Simulation of Shock-Induced Detonation

Experiments were performed to validate the numerical simulation using a detonation-driven shock tube. A schematic of the facility is shown in Fig. 11. The driver tube was highly pressurized initially with helium to 200 atm. The detonation tube was filled with a stoichiometric hydrogen–air mixture to 3 atm. These two tubes were separated by a double-diaphragm section. When the double-diaphragm was ruptured, a shock-induced detonation was set up in the detonation tube. The pressure histories were recorded at several stations on the wall of the detonation tube

12

(PT2–PT5). Figure 12 shows the pressure histories, recorded at stations 4 and 5 corresponding to 166.4 cm and 224.8 cm, respectively, from the location of the downstream diaphragm. The incident detonation wave and the reflected wave were clearly captured at each station. The reflected wave traveled toward the left after reflecting from the diaphragm separating the driven tube and detonation tube. It is interesting to note that the pressure history after arrival of the reflected wave is observed to increase in steps.
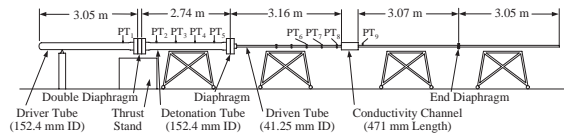

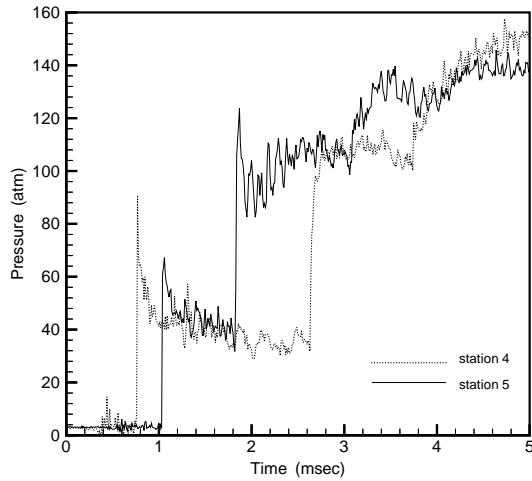Fig.11: Schematic of the UT Arlington detonation-driven shock tube.

Fig.12: Pressure measurements at stations 4 and 5

Numerical modeling of the experiment requires that some assumptions and simplifications be made. For example, the double diaphragm section measured 11.43 cm long and was pressurized initially to 100 atm, about a half of the pressure in the driver tube. Therefore, complex wave interactions may exist inside the double diaphragm section and driver tube until the second diaphragm ruptured and shock-induced detonation was initiated in the detonation tube adjacent to the diaphragm. The details of the double diaphragm rupture were not modeled in the simulation but were replaced by an effective pressure inside the driver tube.

This effective pressure was assumed to act directly on the hydrogen–air mixture in the detonation tube as if the diaphragm was effectively removed at $t = 0$. The effective pressure should be lower than the actual initial pressure in the driver tube but higher than the pressure inside the double diaphragm section. A reasonable first guess for the effective pressure in the driver tube was 150 atm.

Another diaphragm separated the right-end of the detonation tube and the driven tube. The inner diameter of the driven tube was 4.11 cm, much smaller than the 15.24 cm diameter detonation tube. The right-end of the detonation tube is modeled by a reflective boundary based on the fact that the area opening to the driven tube, even after diaphragm rupture, corresponded to only 7 percent of the cross-sectional area of the detonation tube.

Figure 13 shows the resulting pressure histories at stations 4 and 5 from the numerical simulation. The simulation nearly reproduces important features of the experiment, in spite of the assumptions and simplifications used. The arrival time lag in the incident detonation wave between station 4 and 5 is observed to be almost the same as the experimental measurement, which suggests excellent agreement in the detonation wave velocities. The same agreement is observed in the reflected waves. The pressure levels of both incident and reflected waves are also seen to agree well, with the calculated pressure history showed an increase at each station after the arrival of the reflected wave. The step-like pressure rise the simulation almost exactly reproduce the experimental result.
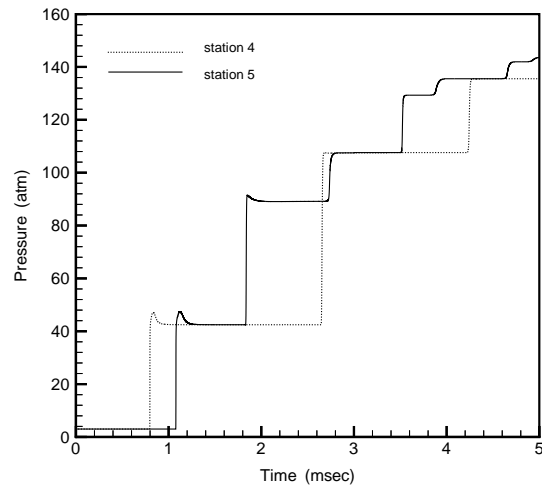

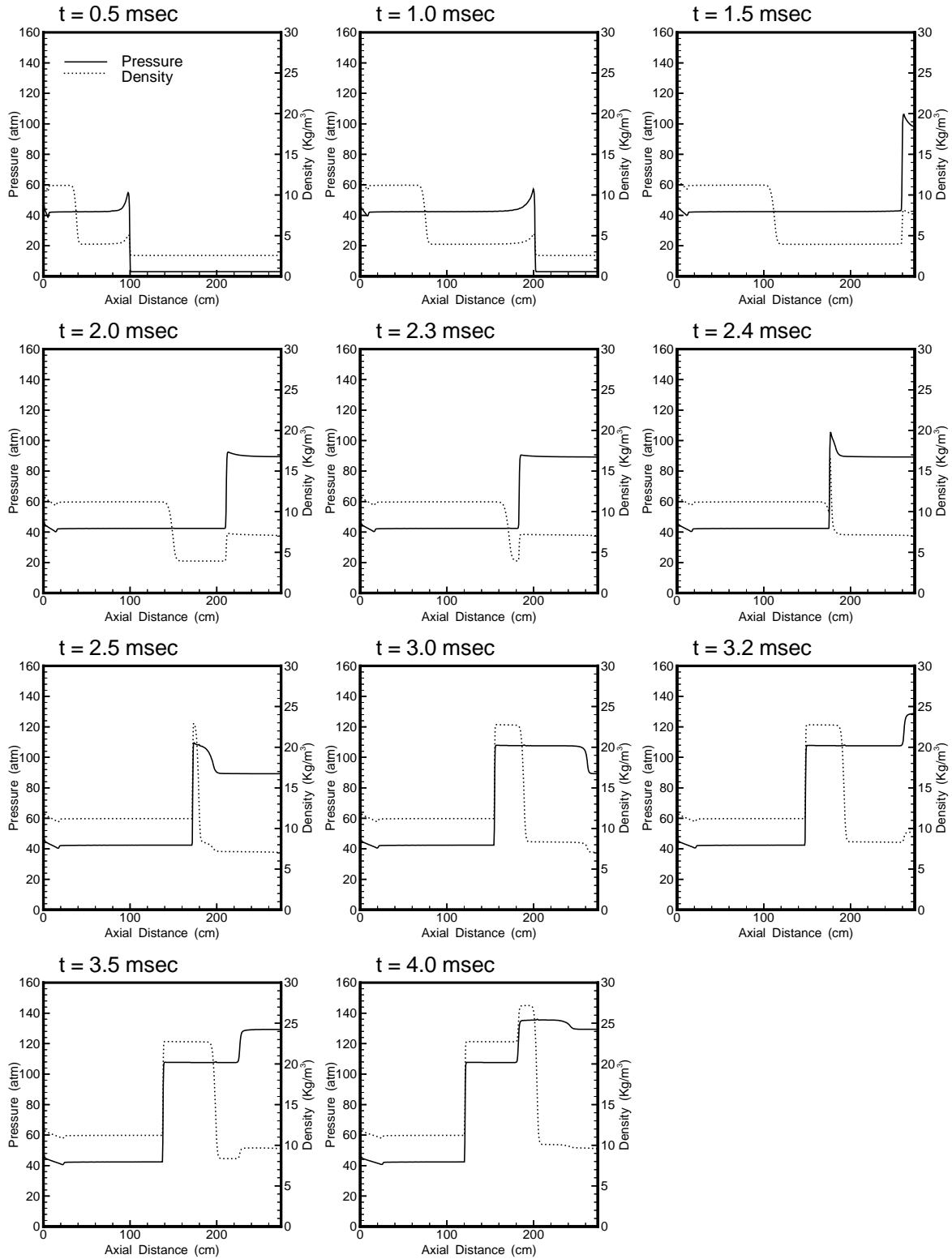Fig.13: Calculated pressure histories at stations 4 and 5.

Fig.14: Wave interations in shock-induced detonation tube.

This step-like pressure history is further examined. Figure 14 shows the evolution of the pressure and density profiles inside the detonation tube. The incident detonation wave is clearly seen to propagate to the right, and the driver material interface is also clearly observed from the density profile to follow the incident wave. The reflection of the incident wave from the right boundary can be seen at 1.5 ms. The reflected wave propagates to the left until it meets the right-running material interface around 2.4 ms. The left-running reflected wave reflects again from the material interface and, as a result, a higher pressure and density are generated from this reflection which propagates back to the right. The material interface travels back toward the left as can be seen after 2.4 ms. The right-running wave reflected from the material interface is observed to reflect once again from the right boundary around 3.1 ms and the resulting shock-increased pressure and density are seen to propagate back to the left. From these observations, the step-like increasing pattern of the pressure history turns out to be a result of these multiple wave reflections.

The simulation result using the current numerical model is in excellent agreement with experimental data. From this observation, the assumptions and the simplifications made to model the experiment are also justified. The use of an effective driver pressure appears to be a reasonable simplification for modeling the double diaphragm section. This simulation validates the current numerical model for calculating the unsteady propagation of a detonation wave and its interactions with boundaries as well as other waves.

5 CONCLUSIONS

A numerical model to simulate hydrogen–air detonation wave propagation and reflection has been presented. For the purpose of constructing an efficient numerical tool to be used in parametric studies, while maintaining a reasonable accuracy to be used for analysis, a two-step global model has been selected and validated for the chemcal reactions of a hydrogen–air mixture. The calculated results from the present model were compared with results from Chapman–Jouguet theory and experimental data. Excellent agreement was observed. The observations validated the efficiency and the accuracy of the present model. Numerical schemes of different order were tested both in temporal and spatial accuracy up to third-order. Mesh convergence tests were performed for different mesh sizes. A second-order accurate scheme in both space and time integration applied to 2.5 mm mesh size seemed to be an appropriate choice from the trade-offs of accuracy and efficiency. Geometry independence of detonation wave properties were also

confirmed as a validation process of the present numerical model. A shock-induced detonation experiment has been simulated. The calculated result almost exactly reproduced the experimental data, and this provided a validation of the present model in the unsteady propagation of a detonation wave.

REFERENCES

[1] Kailasanath, K., "Review of propulsion applications of detonation waves," *AIAA J.*, Vol. 38, No. 9, pp. 1798–1708, 2000.

[2] Lu, F. K., Wilson, D. R., Bakos, R. and Erdos, J. I., "Recent Advances in Detonation Techniques for High-Enthalpy Facilities," *AIAA J.*, Vol. 38, No. 9, pp. 1676-1684, 2000.

[3] Tannehill, J. C., Anderson, D. A. and Pletcher, R. H., *Computational Fluid Mechanics and Heat Transfer*, 2nd ed., Taylor and Francis, 1997.

[4] Gordon, S. and McBride, B. J., "Computer Program for Calculation of Complex Chemical Equilibrium Compositions, Rocket Performance, Incident and Reflected Shocks, and Chapman–Jouguet Detonations," NASA SP-273, 1971.

[5] Gnoffo, P. A., Gupta, R. N. and Shinn, J. L., "Conservation Equations and Physical Models for Hypersonic Air Flows in Thermal and Chemical Nonequilibrium," NASA TP-2867, 1989.

[6] Candler, G. V., "The Computation of Weakly Ionized Hypersonic Flows in Thermo-Chemical Nonequilibrium," Ph.D. Dissertation, Stanford University, June 1988.

[7] Vincenti, W. G. and Kruger, C. H., Jr., *Introduction to Physical Gas Dynamics*, Krieger, Malabar, Florida, 1977.

[8] Millikan, R. C. and White, D. R., "Systematics of Vibrational Relaxation," *J. of Chem. Phys.*, Vol. 39, No. 12, pp. 3209–3213, 1963.

[9] Bussing, T. R. A. and Murman, E. M., "Finite-Volume Method for the Calculation of Compressible Chemically Reacting Flows," *AIAA J.*, Vol. 26, No. 9, pp. 1070–1078, 1988.

[10] Roe, P. L., "Approximate Riemann Solvers, Parameter Vectors, and Difference Schemes," *J. Comput. Phys.*, Vol. 43, No. 2, pp. 357–372, 1981.

[11] Grossman, B. and Cinnella P., "Flux-Split Algorithms for Flows with Non-equilibrium Chemistry and Vibrational Relaxation," *J. of Comp. Phys.*, Vol. 88, No. 1, pp. 131–168, 1990.

[12] Munipalli, R., Kim, H., Anderson, D. A. and Wilson D. R., "Computation of Unsteady Nonequilibrium Propulsive Flowfields," AIAA Paper 97–2704, 1997.

[13] Rogers, R. C. and Chinitz, W., "Using a Global Hydrogen–Air Combustion Model in Turbulent Reacting Flow Calculations," *AIAA J.*, Vol. 21,

No. 4, pp. 586–592, 1983.

[14] Gordon, S. and McBride, B. J., "Computer Program for Calculation of Complex Chemical Equilibrium Compositions and Applications – I. Analysis," NASA RP-1311, October 1994; http://www.grc.nasa.gov/WWW/CEAWeb/xWhatCEA.htm.

[15] Lu, F. K., Kim, C. H., Wilson, D. R., Liu, H. C., Stuessy, W. S. and Simmons, G. A., "Exploratory Study of Conductivity in Detonation Waves," AIAA Paper 99–0868, 1999.